

Resonant absorption and linear photovoltaic effect in ferroelectric moiré heterostructures

V. V. Enaldiev^{1, 2, 3, *} and Z. Z. Alisultanov^{1, 4, †}

¹*Moscow Center for Advanced Studies, Kulakova str. 20, Moscow 123592, Russia*

²*Kotelnikov Institute of Radio-engineering and Electronics of the RAS, Mokhovaya 11-7, Moscow 125009, Russia*

³*HSE University, Moscow, 101000 Russia*

⁴*Institute of Physics of DFRS of the RAS, Makhachkala, 367015, Russia*

Twisted bilayers, featuring interfacial ferroelectricity in the form of array of polar domains, combined with incommensurate two-dimensional layers in a single van der Waals heterostructures allows for generation of purely electrostatic moiré superlattice potentials in the latter. We study electronic and optoelectronic properties of such heterostructures composed of graphene stacked with the twisted ferroelectric bilayers and show that doping of graphene substantially affects mini-band structures because of screening of free carriers. We demonstrate that formation of van Hove singularities in density of states modifies linear and second-order responses of the structures leading to resonant absorption and linear photovoltaic effect, respectively. The latter is generated solely by a shift photocurrent, arising only with account of virtual optical transitions, whereas an injection photocurrent is forbidden by symmetry.

Van der Waals (vdW) heterostructures containing moiré superlattices at twisted interfaces are at the forefront of solid-state physics and material science, motivated by discoveries of superconductivity in twisted WSe₂ [1, 2] and graphene [3–5] bilayers, strongly correlated [6, 7] and other exotic [8] phases in bi-, and tri-layer [9, 10] structures, as well as interfacial ferroelectricity in twisted hexagonal boron nitride [11–14] (hBN) and transition metal dichalcogenides [15, 16] (TMD) bilayers.

The interfacial ferroelectricity is a novel type of ferroelectric order specific to layered vdW materials where electric dipole moments are bounded to stacking arrangements of the layers [17]. In the twisted hBN and TMD heterostructures it emerges as an array of triangular domains characterized by the out-of-plane electric polarization, which scales linearly with the number of twisted interfaces [18–20] and can be switched via domain wall sliding [21–25].

Integrating an interfacial ferroelectric with a functional layer in a single vdW heterostructure enables the creation of a purely electrostatic moiré superlattice potential in the functional layer [26, 27]. This potential has been recently studied experimentally through electron [28, 29] and exciton [30] transport. A distinctive feature of such an electrostatic moiré potential, compared to those resulting from interlayer hybridisation in commensurate twistronic structures, is its tunability via free-carrier and proximate electrostatic gate screening as well as out-of-plane electric fields that reshape the underlying ferroelectric domains [15, 21, 22, 24].

In the Letter, we demonstrate that an electrostatic moiré superlattice potential, arising from polar domains, generates mini-bands for massless Dirac fermions (mDF)

in graphene with dispersion controllable by variation of carrier concentration at the fixed moiré superlattice period. In addition, mini-band formation leads to a substantial enhancement of graphene's optical absorption up to $\approx 10\%$ at resonant frequencies that correspond to allowed optical transitions between states at van Hove singularities (vHS). Furthermore, we show that the mini-band structure, combined with lack of inversion symmetry in the heterostructure produces linear photovoltaic effect [31–34] that is purely driven by a shift photocurrent; an injection current is absent by symmetry. Both the linear and second-order optical responses are tunable via twist angle, electron doping and an out-of-plane electric field applied across the twisted interface.

Using periodicity of the moiré superlattice in the twisted bilayer we express the electrostatic moiré potential in graphene from polar domains as a Fourier series:

$$V(\mathbf{r}) = V_0^{(s)} + \sum_{\substack{l=1,2,3, \dots \\ j=1,2,3}} V_l^{(s)} \cos(\mathbf{g}_j^{(l)} \cdot \mathbf{r}) + V_l^{(a)} \sin(\mathbf{g}_j^{(l)} \cdot \mathbf{r}). \quad (1)$$

Here $V_l^{(s)}$ and $V_l^{(a)}$ are real Fourier amplitudes of the potential that depend on the carrier concentration in graphene, dielectric environment, and gate proximity (see section S1 in Supplementary Materials (SM)), vectors $\mathbf{g}_{1,2,3}^{(l)}$ form the l -th triad of moiré superlattice reciprocal vectors related by 120°-rotation. Note, that placing the electrostatic gate near the twisted interface – but on the side opposite to graphene layer – doubles the electrostatic moiré superlattice potential in graphene compared to the case of remote gate [26]. For an ideal moiré superlattice with 120°-rotational symmetry, the zeroth and even-order Fourier amplitudes arise only in presence of a finite out-of-plane electric field, which creates an area imbalance between domains of opposite polarisation [15, 21, 24].

* vova.enaldiev@gmail.com
† zaur0102@gmail.com

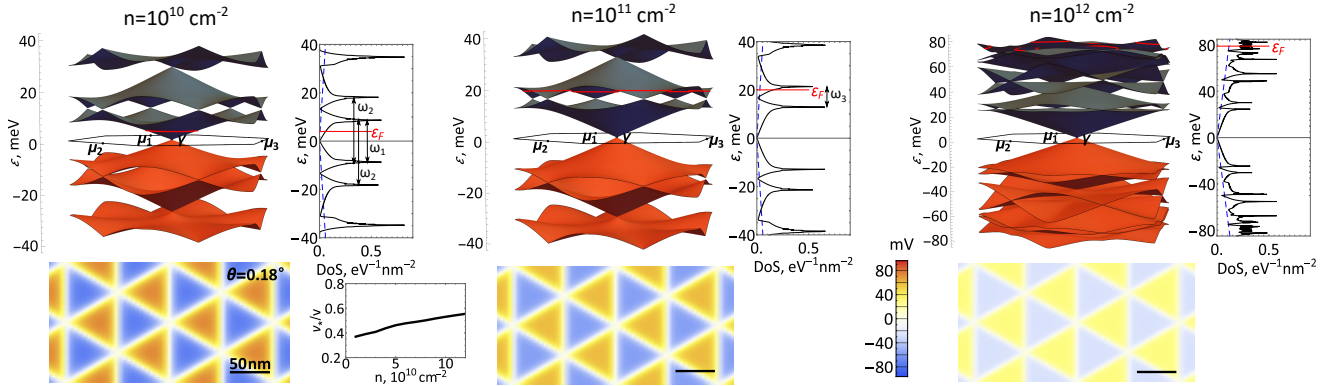


Figure 1. Low-energy mini-bands and corresponding densities of states for graphene/twisted hBN bilayer heterostructure characterized by twist angle $\theta = 0.18^\circ$ for three values of electron doping $n = 10^{10}, 10^{11}$ and 10^{12} cm^{-2} (red lines show corresponding Fermi-energies ε_F). Blue dashed line shows density of states in an isolated graphene; arrows indicate resonant frequencies in absorption. Bottom insets show distribution of electrostatic moiré potential in graphene created by polar domains in twisted hBN bilayer and renormalization of primary mDF group velocity with electron concentration at $\theta = 0.18^\circ$.

We begin with calculation of a mini-band structure for free carriers in graphene with potential (1) which reduces to solution of the following equation [35, 36]:

$$\hat{H}\psi = \varepsilon\psi, \quad (2)$$

$$\hat{H} = v\boldsymbol{\sigma} \cdot \hat{\mathbf{p}} + V(\mathbf{r}), \quad (3)$$

where $\psi = (\psi_1, \psi_2)^T$ and $v \approx 10^6 \text{ m/s}$ are a two-component envelope wave function and the speed of Dirac fermions in graphene, respectively, $\boldsymbol{\sigma} = (\sigma_x, \sigma_y)$ is 2D vector of the Pauli matrices acting in sublattice space, $\hat{\mathbf{p}} = -i\hbar(\partial/\partial x, \partial/\partial y)$ is the quasi-momentum operator. Eq. (2) can be diagonalized in the basis of Bloch functions $\psi_{n,\mathbf{k}} = e^{i\mathbf{q}\mathbf{r}}u_{n,\mathbf{k}}(\mathbf{r})$ corresponding to eigen values $\varepsilon_n(\mathbf{k})$, where $u_{n,\mathbf{k}}(\mathbf{r})$ is a moiré periodic Bloch amplitude characterized by the miniband index, $n = 1, 2, 3, \dots$ for electrons ($n = -1, -2, -3, \dots$ for holes), and a quasi-momentum, \mathbf{k} , defined in moiré Brillouin zone (mBZ).

Since an account of finite out-of-plane electric field does not change results obtained for zero electric field, in the main text we focus on the latter case. The corresponding results for a finite field are gathered in sections S4 and S5 of SM. In the absence of the out-of-plane electric field the moiré potential (1) possesses odd parity, $V(-\mathbf{r}) = -V(\mathbf{r})$, illustrated on the bottom insets in Fig. S5 ($V_l^{(s)} \equiv 0$, $l = 0, 1, 2, \dots$). The operator \hat{I} , transforming $\mathbf{r} \rightarrow -\mathbf{r}$, then, corresponds to the chiral symmetry of Hamiltonian (3), satisfying $\hat{H}\hat{I} = -\hat{I}\hat{H}$. Combined with an intravalley hidden symmetry $\hat{T} = i\sigma_y\hat{K}$ (where \hat{K} is the complex conjugation operator and $\hat{H}\hat{T} = \hat{T}\hat{H}$), this leads to electron-hole symmetry of states with the same quasi-momentum: $\varepsilon_n(\mathbf{k}) = -\varepsilon_{-n}(\mathbf{k})$. We also note that the Hamiltonian (3) is invariant under non-centrosymmetric C_{3v} point group, which includes, in particular, mirror reflection with respect to the y -axis, represented by an operator, $\hat{M}_y = \sigma_x\{y \rightarrow -y\}$ used below.

In Fig. S5 we demonstrate the dispersions obtained for several values of graphene doping, calculated with the

help of expansion of $u_{n,\mathbf{k}}(\mathbf{r})$ in Fourier series and diagonalization of the resulting matrix for all quasimomenta \mathbf{k} in mBZ, with the number of harmonics large enough to satisfy convergence in the low-energy spectral interval. The lowest mini-bands ($n = \pm 1$) are characterised by gapless spectrum at the neutrality point ($\varepsilon = 0$) as the electrostatic moiré potential does not break the sublattice symmetry required to produce a gap for mDF. However, the group velocity of $n = \pm 1$ minibands can be substantially suppressed by the moiré potential. To demonstrate this we project out Eq. (1) to a subspace of the two degenerate states $\psi_{\pm 1,\mathbf{k}=0}$ and perturbatively account for $v\boldsymbol{\sigma} \cdot \mathbf{k}$. Then, leaving in Fourier series for $u_{\pm 1,\mathbf{k}=0}$ only the zeroth and $\pm \mathbf{g}_{1,2,3}^{(1)}$ harmonics, we obtain the following effective Hamiltonian (see section S2 in SM):

$$H_\gamma = \hbar v_* \boldsymbol{\sigma} \cdot \mathbf{k}, \quad (4)$$

characterised by the renormalized group velocity

$$v_* = \frac{v}{1 + \left(\frac{3V_1^{(a)}a}{4\sqrt{2}\pi\hbar v\theta} \right)^2}. \quad (5)$$

From Eq. (5) it follows that v_* is a function of both moiré superlattice period ($\approx a/\theta$) and, implicitly, free carrier density via $V_1^{(a)}$. Unlike graphene/hBN moiré superlattices [37, 38] or periodically patterned graphene [39, 40] where renormalization of the primary mDF velocity is small, here, decrease of v_* can be as large as ≈ 3 times for realistic parameters (see bottom inset in Fig. S5). Opportunity to tune the mDF velocity can have practical significance for adjusting transmission probability of p-n junctions [41] in the heterostructures, whereas its reduction may help to observe Landau level breakdown even at moderate homogeneous electric fields [42, 43].

At $\mathbf{k} = \mathbf{g}_{1,2,3}^{(1)}/2 \equiv \boldsymbol{\mu}_{1,2,3}$ located at the mBZ edges, pairs of electron ($n = 1$ and $n = 2$) and hole ($n = -1$

and $n = -2$) mini-bands become degenerate, forming secondary Dirac points symmetrically with respect to $\varepsilon = 0$. Around the degeneracy momenta, $\mathbf{q} = \mathbf{k} - \boldsymbol{\mu}_i$, an effective model can be constructed accounting for coupling of the two harmonics $|\boldsymbol{\mu}_i + \mathbf{q}\rangle$ and $|\boldsymbol{\mu}_i + \mathbf{q} - \mathbf{g}_i\rangle$ in the Fourier expansion of $u_{\boldsymbol{\mu}_i + \mathbf{q}}$, which leads to [44] (see section S3 in SM):

$$H_{\boldsymbol{\mu}_3}^{(\pm)} = \pm \left(\varepsilon_{\boldsymbol{\mu}} + \frac{(\hbar v_*)^4 g^2}{8\varepsilon_{\boldsymbol{\mu}}^3} q_y^2 \right) \sigma_0 \pm \frac{V_1^{(a)} \hbar v_*}{2\varepsilon_{\boldsymbol{\mu}}} q_y \sigma_z - \hbar v_* q_x \sigma_x, \quad (6)$$

where $+/ -$ sign is for electrons/holes, $\pm \varepsilon_{\boldsymbol{\mu}} = \pm \sqrt{(\hbar v_* g)^2 + (V_1^{(a)})^2} / 2$ are energies of the secondary Dirac points ($g = |\mathbf{g}_1^1|$), and σ_0 is an identity matrix. Hamiltonian (6) gives rise to strongly anisotropic mDF (see Fig. S5), where in contrast to graphene/hBN [37, 38, 45] or patterned graphene [39] velocities in both principal axes can be controlled by carrier concentration and twist angle.

Increasing the doping level, the Fermi contour undergo Lifshitz transition shifting from a central γ pocket to those in $\mu_{1,2,3}$ followed by the formation of a pair of vHS in density of states (DOS). We reveal below that the formation of these electron-hole symmetric vHS significantly modifies both the linear and second-order responses of the system in infrared energy range.

We consider normal incidence of a plane monochromatic electromagnetic wave, described by vector-potential $\mathbf{A}(\mathbf{r}, t) = A_0 \boldsymbol{\eta} \cos(kz - \omega t)$, where A_0 and $\boldsymbol{\eta} = (\cos \chi, \sin \chi, 0)$ characterize the amplitude and polarisation of the wave, respectively. Using first-order perturbation theory, the interband absorption coefficient is expressed as follows [46] (in SI units):

$$\alpha(\omega) = \frac{g_s g_v \pi e^2}{c \omega \epsilon_0 S} \sum_{n,n'} |(\hat{\mathbf{v}}_{nn'}(\mathbf{k}) \cdot \boldsymbol{\eta})|^2 [f_{n',\mathbf{k}} - f_{n,\mathbf{k}}] \delta(\varepsilon_{n,\mathbf{k}} - \varepsilon_{n',\mathbf{k}} - \hbar\omega), \quad (7)$$

where $g_s = 2$ and $g_v = 2$ are the spin and valley degeneracy factors in graphene, c is speed of light, ϵ_0 is the dielectric permittivity of vacuum, S is the area of the structure, n, n' are the mini-band indexes, $\hat{\mathbf{v}}_{nn'}(\mathbf{k})$ is interband matrix element of velocity operator $\hat{\mathbf{v}} = \partial H / \partial \hat{p} = v\boldsymbol{\sigma}$ on the Bloch states characterised by quasi-momentum \mathbf{k} , and $f_{n/n',\mathbf{k}} \equiv f(\varepsilon_{n/n',\mathbf{k}})$ are the Fermi-Dirac distribution functions characterised by equilibrium for given electron density.

The $\alpha(\omega)$ dependences, displayed in Fig. 2 for $\theta = 0.18^\circ$, exhibit resonances whose frequencies depend on the filling of mini-band structure. At an electron concentration of $n = 10^{10} \text{ cm}^{-2}$ (corresponding to filling of $n = 1$ mini-band before the Lifshitz transition, left panel in Fig. S5), the absorption coefficient is dominated by three terms in Eq. (7): $(n', n) = (-1, 1), (-1, 2)$ and

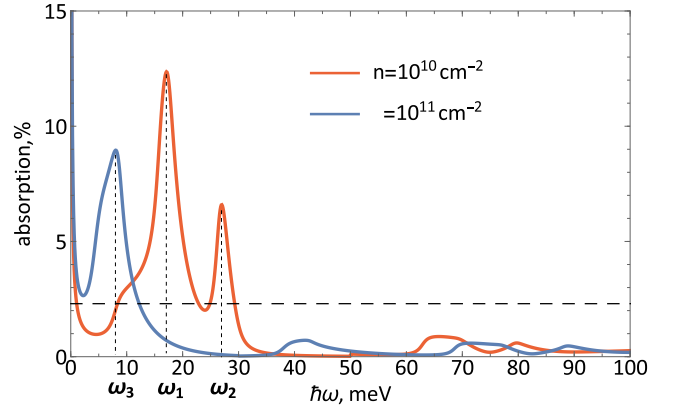


Figure 2. Frequency dependences of the absorption coefficient (7) for doping levels corresponding to Fig. S5 at $T \ll \hbar\omega_3$. The resonances, $\omega_{1,2,3}$, corresponds to energy differences between states at peaks of DOS, shown in Fig. S5, where the interband velocity matrix elements are non-zero. Dashed line indicates absorption (2.3%) of an isolated graphene layer [47].

($-2, 1$). The first term accounts for the peak at ω_1 , while the latter two contribute equally to the peak at ω_2 .

At a higher concentration, $n = 10^{11} \text{ cm}^{-2}$ (middle panel in Fig. S5), transitions between electron and hole mini-bands are suppressed by Pauli blocking, whereas transition between electron $n' = 1$ and $n = 2$ mini-bands become activated in Eq. (7), resulting in a peak at frequency ω_3 . In both cases, the resonances arise from allowed optical transitions from filled states at one vHS to empty states of another vHS forming close to the boundary of mid- and far-infrared range.

We note that the magnitude of absorption at these resonances can significantly exceed that of an individual graphene layer [47] (dashed line in Fig. 2), making it competitive with plasmon absorption of graphene nanostructures [48].

To observe the resonant absorption, the temperature should satisfy $T \ll \hbar\omega_{1,2,3}$ to ensure complete population and depletion of the corresponding vHS responsible for each resonance. For the case of $\theta = 0.18^\circ$, shown in Fig. 2, this requires cryogenic temperatures for every resonance. However, since quasi-momentum states of $n = \pm 1, \pm 2$ minibands, that form vHS, lie near the mBZ edge, the resonance frequencies – particularly $\omega_{1,2}$ – can be readily tuned by adjusting θ . This allows the condition to be met even at room temperatures for larger twist angles, with the shift of resonance frequency deeper into the mid-infrared range.

Now, we consider second order response and show the emergence of the linear photovoltaic effect [31, 32] associated with resonant shift photocurrent. To this end, solving the quantum kinetic equation (see details in SM), we find second order amendment to the single-particle density matrix on the incident wave amplitude, $\rho^{(2)} \propto A_0^2$,

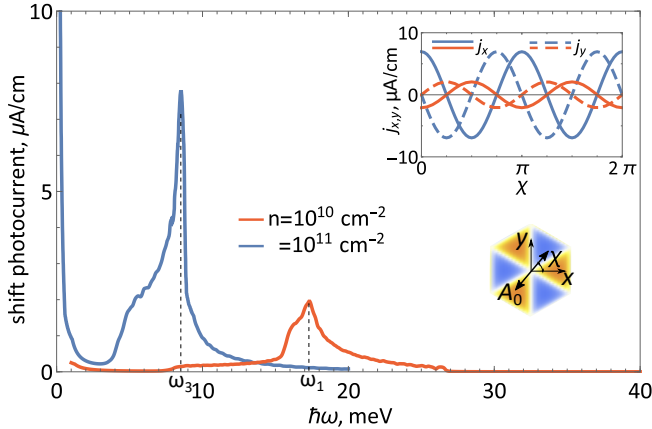


Figure 3. Frequency dependences of the shift photocurrent (10) for graphene-twisted hBN bilayer with $\theta = 0.18^\circ$ at the intensity of the incident radiation $I = 0.1\text{W/cm}^2$ and indicated electron dopings. Insets: (Top) Dependences of $j_{\text{shift}}^{x,y}(\omega_1, \chi)$ (red) and $j_{\text{shift}}^{x,y}(\omega_3, \chi)$ (blue) on the polarisation of the incident electromagnetic wave, characterised by angle χ . (Bottom) Orientation of the polarisation with respect to moiré superlattice in the twisted bilayer.

and then, calculate photocurrent as follows:

$$\mathbf{j} = \frac{1}{S} \text{Tr}(e\hat{\mathbf{v}}\rho^{(2)}) = \mathbf{j}_{\text{inj}} + \mathbf{j}_{\text{shift}}. \quad (8)$$

Here Tr denotes operator trace, the first term on the right hand side describes an injection photocurrent

$$\mathbf{j}_{\text{inj}} = \frac{g_s g_v \pi e^3 I \tau}{\hbar c \epsilon_0 \omega^2 S} \sum_{\substack{n, n' \\ \mathbf{k}, s = \pm}} [f_{n'} - f_n] \delta(\epsilon_n - \epsilon_{n'} - s\hbar\omega) \times \hat{\mathbf{v}}_{nn}(\hat{\mathbf{v}}_{nn} \cdot \boldsymbol{\eta})(\hat{\mathbf{v}}_{n'n} \cdot \boldsymbol{\eta}), \quad (9)$$

whereas the second is a shift photocurrent

$$\mathbf{j}_{\text{shift}} = \frac{g_s g_v \pi e^3 I}{c \epsilon_0 \omega^2 S} \sum_{\substack{n, n', n'' \neq n \\ \mathbf{k}, s = \pm}} [f_{n'} - f_n] \delta(\epsilon_n - \epsilon_{n'} - s\hbar\omega) \times \text{Im} \left[\frac{\hat{\mathbf{v}}_{n'n''}(\hat{\mathbf{v}}_{n''n} \cdot \boldsymbol{\eta})(\hat{\mathbf{v}}_{nn'} \cdot \boldsymbol{\eta})}{\epsilon_{n''} - \epsilon_n} \right]. \quad (10)$$

In Eqs. (9) and (10) $I = c\epsilon_0\omega^2 A_0^2/2$ is the incident wave intensity, τ is a phenomenological momentum relaxation time and \mathbf{k} is suppressed in arguments of matrix elements and energy values. The hidden intravalley symmetry, \hat{T} of the Hamiltonian (2) leads to the following relation [49]:

$$\mathbf{v}_{nn'}(\mathbf{k}) = -e^{i[\alpha_{n'}(\mathbf{k}) - \alpha_n(\mathbf{k})]} \mathbf{v}_{nn'}^*(-\mathbf{k}), \quad (11)$$

which has already been used in derivation of Eq. (10) ($\alpha_{n'}(\mathbf{k})$ and $\alpha_n(\mathbf{k})$ are arbitrary gauge phases). Self-conjugation of $\hat{\mathbf{v}}$ supplemented with Eq. (11) and $\epsilon_{n,\mathbf{k}} =$

$\epsilon_{n,-\mathbf{k}}$ leads to vanishing of the injection current (9) independently on the polarisation of the wave. We note that account of small trigonal warping terms in Hamiltonian (2) would only lead to a valley-polarised injection photocurrent as in isolated graphene layer [50], whereas a net contribution of $+K$ and $-K$ valleys would compensate each other [51].

Nevertheless, the shift photocurrent (10) is non-zero and exhibits resonances at ω_1 or ω_3 depending on the carrier density, as shown in Fig. 3. However, the shape of the resonances as a function of frequency differs from that of the absorption coefficient. The latter arises from real interband transitions between states that satisfy energy conservation, $\epsilon_{n,\mathbf{k}} - \epsilon_{n',\mathbf{k}} - \hbar\omega$. In contrast, the shift photocurrent relies crucially on virtual interband transitions, which do not require energy conservation for the intermediate states.

Indeed, by restricting the summation in Eq. (10) to n and n' bands satisfying energy conservation in the delta-function (i.e. retaining only terms with $n'' = n$ for arbitrary n, n') and, for definiteness, specifying polarisation $\boldsymbol{\eta} \parallel O_x$ we obtain

$$j_{\text{shift}}^x = \sum_{\mathbf{k}} F(\epsilon_n, \epsilon'_n) \text{Im} \left[|\hat{v}_{n'n}^x(\mathbf{k})|^2 \hat{v}_{nn}(\mathbf{k}) \right] = 0, \quad (12)$$

$$j_{\text{shift}}^y = \sum_{\mathbf{k}} F(\epsilon_n, \epsilon'_n) \text{Im} [\hat{v}_{n'n}^y(\mathbf{k}) \hat{v}_{nn'}^x(\mathbf{k}) \hat{v}_{nn}^x(\mathbf{k})] = 0, \quad (13)$$

where $F(\epsilon_n, \epsilon'_n)$ contains only energy-dependent factors from Eq. (10) invariant under C_{3v} point group symmetry. Therefore, the vanishing of j_{shift}^x (12) occurs because group velocity $\hat{v}_{nn}(\mathbf{k}) = \partial\epsilon_n(\mathbf{k})/\partial\mathbf{k}$ is real. On the other hand, mirror symmetry, \hat{M}_y , of the Hamiltonian (2) leads to $\hat{v}_{n'n}^y(k_x, -k_y) = -\hat{v}_{n'n}^y(k_x, k_y)$, $\hat{v}_{n'n}^x(k_x, -k_y) = \hat{v}_{n'n}^x(k_x, k_y)$, equalizing the sum over \mathbf{k} in Eq. (13) to zero.

These arguments demonstrate that the existence of more than two bands coupled via velocity matrix elements is a necessary condition for emergence of the shift photocurrent in the heterostructure, which is a distinctive feature of the photovoltaic effect in pure crystals [31, 32].

On the inset in Fig. 3 we show polarisation dependence of the photocurrent at resonant frequencies, $j_{\text{shift}}(\chi) \propto (\cos 2\chi, -\sin 2\chi)$ specific for C_{3v} point group [52].

Finally, we discuss the effect of an out-of-plane electric field across the twisted bilayer. While such a field breaks the chiral symmetry of \hat{H} by modifying the domain structure [15, 21], it does not eliminate van Hove singularities in density of states. Therefore, the resonant responses persists at finite out-of-plane electric field that provides an additional external tool to control the resonant conditions. Moreover, since the electric field preserves \hat{T} and the spatial symmetries, the photovoltaic effect remains governed by the shift photocurrent, while the injection current also vanishes.

We believe that the resonant linear photovoltaic effect

should not be exclusive to moiré potential of polar domains in graphene, but is also likely present in bilayer graphene and within the intrinsic electron/hole minibands of twisted TMD bilayers characterized by broken inversion symmetry and vHS [26].

Acknowledgements. We thank Denis Bandurin for

fruitful discussions. The work was supported by the Russian Science Foundation (main text) (project No. 24-72-10015) and Ministry of Science and Higher Education of the Russian Federation (results for finite out-of-plane electric field in Supplementary Materials) (No. FSMG-2026-0012).

[1] Y. Xia, Z. Han, K. Watanabe, T. Taniguchi, J. Shan, and K. F. Mak, Superconductivity in twisted bilayer wse2, *Nature* **637**, 833 (2024).

[2] Y. Guo, J. Pack, J. Swann, L. Holtzman, M. Cothrine, K. Watanabe, T. Taniguchi, D. G. Mandrus, K. Barmak, J. Hone, A. J. Millis, A. Pasupathy, and C. R. Dean, Superconductivity in 5.0° twisted bilayer wse2, *Nature* **637**, 839 (2025).

[3] Y. Cao, V. Fatemi, S. Fang, K. Watanabe, T. Taniguchi, E. Kaxiras, and P. Jarillo-Herrero, Unconventional superconductivity in magic-angle graphene superlattices, *Nature* **556**, 43 (2018).

[4] X. Lu, P. Stepanov, W. Yang, M. Xie, M. A. Aamir, I. Das, C. Urgell, K. Watanabe, T. Taniguchi, G. Zhang, *et al.*, Superconductors, orbital magnets and correlated states in magic-angle bilayer graphene, *Nature* **574**, 653 (2019).

[5] M. Yankowitz, S. Chen, H. Polshyn, Y. Zhang, K. Watanabe, T. Taniguchi, D. Graf, A. F. Young, and C. R. Dean, Tuning superconductivity in twisted bilayer graphene, *Science* **363**, 1059 (2019).

[6] L. Wang, E.-M. Shih, A. Ghiotto, L. Xian, D. A. Rhodes, C. Tan, M. Claassen, D. M. Kennes, Y. Bai, B. Kim, K. Watanabe, T. Taniguchi, X. Zhu, J. Hone, A. Rubio, A. N. Pasupathy, and C. R. Dean, Correlated electronic phases in twisted bilayer transition metal dichalcogenides, *Nature Materials* **19**, 861 (2020).

[7] E. Li, J.-X. Hu, X. Feng, Z. Zhou, L. An, K. T. Law, N. Wang, and N. Lin, Lattice reconstruction induced multiple ultra-flat bands in twisted bilayer wse2, *Nature Communications* **12**, 10.1038/s41467-021-25924-6 (2021).

[8] D. Bandurin, A. Principi, I. Phinney, T. Taniguchi, K. Watanabe, and P. Jarillo-Herrero, Interlayer electron-hole friction in tunable twisted bilayer graphene semimetal, *Physical Review Letters* **129**, 206802 (2022).

[9] S. Xu, M. M. Al Ezzi, N. Balakrishnan, A. Garcia-Ruiz, B. Tsim, C. Mullan, J. Barrier, N. Xin, B. A. Piot, T. Taniguchi, K. Watanabe, A. Carvalho, A. Mishchenko, A. K. Geim, V. I. Fal'ko, S. Adam, A. H. C. Neto, K. S. Novoselov, and Y. Shi, Tunable van hove singularities and correlated states in twisted monolayer–bilayer graphene, *Nature Physics* **17**, 619 (2021).

[10] S. Chen, M. He, Y.-H. Zhang, V. Hsieh, Z. Fei, K. Watanabe, T. Taniguchi, D. H. Cobden, X. Xu, C. R. Dean, *et al.*, Electrically tunable correlated and topological states in twisted monolayer–bilayer graphene, *Nature Physics* **17**, 374 (2021).

[11] C. Woods, P. Ares, H. Nevison-Andrews, M. Hollwill, R. Fabregas, F. Guinea, A. Geim, K. Novoselov, N. Walet, and L. Fumagalli, Charge-polarized interfacial superlattices in marginally twisted hexagonal boron nitride, *Nature communications* **12**, 1 (2021).

[12] M. V. Stern, Y. Waschitz, W. Cao, I. Nevo, K. Watanabe, T. Taniguchi, E. Sela, M. Urbakh, O. Hod, and M. B. Shalom, Interfacial ferroelectricity by van der Waals sliding, *Science* **372**, 1462 (2021).

[13] K. Yasuda, X. Wang, K. Watanabe, T. Taniguchi, and P. Jarillo-Herrero, Stacking-engineered ferroelectricity in bilayer boron nitride, *Science* **372**, 1458 (2021).

[14] E. Pan, Z. Li, F. Yang, K. Niu, R. Bian, Q. Liu, J. Chen, B. Dong, R. Wang, T. Zhou, A. Zhou, X. Luo, J. Chu, J. Lin, W. Li, and F. Liu, Observation and manipulation of two-dimensional topological polar texture confined in moiré interface, *Nature Communications* **16**, 10.1038/s41467-025-58105-w (2025).

[15] A. Weston, E. G. Castanon, V. Enaldiev, F. Ferreira, S. Bhattacharjee, S. Xu, H. Corte-León, Z. Wu, N. Clark, A. Summerfield, T. Hashimoto, Y. Gao, W. Wang, M. Hamer, H. Read, L. Fumagalli, A. V. Kretinin, S. J. Haigh, O. Kazakova, A. K. Geim, V. I. Fal'ko, and R. Gorbachev, Interfacial ferroelectricity in marginally twisted 2d semiconductors, *Nature Nanotechnology* **10**, 10.1038/s41565-022-01072-w (2022).

[16] X. Wang, K. Yasuda, Y. Zhang, S. Liu, K. Watanabe, T. Taniguchi, J. Hone, L. Fu, and P. Jarillo-Herrero, Interfacial ferroelectricity in rhombohedral-stacked bilayer transition metal dichalcogenides, *Nature Nanotechnology* **17**, 367 (2022).

[17] M. Vizner Stern, S. Salleh Atri, and M. Ben Shalom, Sliding van der waals polytypes, *Nature Reviews Physics* **7**, 50 (2024).

[18] S. Deb, W. Cao, N. Raab, K. Watanabe, T. Taniguchi, M. Goldstein, L. Kronik, M. Urbakh, O. Hod, and M. Ben Shalom, Cumulative polarization in conductive interfacial ferroelectrics, *Nature* **612**, 465 (2022).

[19] M. Van Winkle, N. Dowlatshahi, N. Khaloo, M. Iyer, I. M. Craig, R. Dhall, T. Taniguchi, K. Watanabe, and D. K. Bediako, Engineering interfacial polarization switching in van der waals multilayers, *Nature Nanotechnology* **19**, 751 (2024).

[20] F. Ferreira, V. V. Enaldiev, and V. I. Fal'ko, Scalability of dielectric susceptibility ϵ_{zz} with the number of layers and additivity of ferroelectric polarization in van der waals semiconductors, *Physical Review B* **106**, 125408 (2022).

[21] V. V. Enaldiev, F. Ferreira, and V. I. Fal'ko, A scalable network model for electrically tunable ferroelectric domain structure in twistronic bilayers of two-dimensional semiconductors, *Nano Letters* **22**, 1534 (2022).

[22] L. Molino, L. Aggarwal, V. Enaldiev, R. Plumadore, V. I. Fal'ko, and A. Luican-Mayer, Ferroelectric switching at symmetry-broken interfaces by local control of dislocations networks, *Advanced Materials* **35**, 10.1002/adma.202207816 (2023).

[23] J. Liang, D. Yang, Y. Xiao, S. Chen, J. I. Dadap, J. Rot

tler, and Z. Ye, Shear strain-induced two-dimensional slip avalanches in rhombohedral MoS₂, *Nano Letters* **23**, 7228 (2023).

[24] K. Ko, A. Yuk, R. Engelke, S. Carr, J. Kim, D. Park, H. Heo, H.-M. Kim, S.-G. Kim, H. Kim, T. Taniguchi, K. Watanabe, H. Park, E. Kaxiras, S. M. Yang, P. Kim, and H. Yoo, Operando electron microscopy investigation of polar domain dynamics in twisted van der waals heterobilayers, *Nature Materials* **22**, 992 (2023).

[25] R. Bian, R. He, E. Pan, Z. Li, G. Cao, P. Meng, J. Chen, Q. Liu, Z. Zhong, W. Li, and F. Liu, Developing fatigue-resistant ferroelectrics using interlayer sliding switching, *Science* **385**, 57 (2024).

[26] S. J. Magorrian, V. V. Enaldiev, V. Zólyomi, F. Ferreira, V. I. Fal'ko, and D. A. Ruiz-Tijerina, Multifaceted moiré superlattice physics in twisted WSe₂ bilayers, *Physical Review B* **104**, 125440 (2021).

[27] P. Zhao, C. Xiao, and W. Yao, Universal superlattice potential for 2d materials from twisted interface inside h-bn substrate, *npj 2D Materials and Applications* **5**, 10.1038/s41699-021-00221-4 (2021).

[28] J. Ding, H. Xiang, W. Zhou, N. Liu, Q. Chen, X. Fang, K. Wang, L. Wu, K. Watanabe, T. Taniguchi, N. Xin, and S. Xu, Engineering band structures of two-dimensional materials with remote moiré ferroelectricity, *Nature Communications* **15**, 9087 (2024).

[29] X. Wang, C. Xu, S. Aronson, D. Bennett, N. Paul, P. J. D. Crowley, C. Collignon, K. Watanabe, T. Taniguchi, R. Ashoori, E. Kaxiras, Y. Zhang, P. Jarillo-Herrero, and K. Yasuda, Moiré band structure engineering using a twisted boron nitride substrate, *Nature Communications* **16**, 10.1038/s41467-024-55432-2 (2025).

[30] D. S. Kim, R. C. Dominguez, R. Mayorga-Luna, D. Ye, J. Embley, T. Tan, Y. Ni, Z. Liu, M. Ford, F. Y. Gao, S. Arash, K. Watanabe, T. Taniguchi, S. Kim, C.-K. Shih, K. Lai, W. Yao, L. Yang, X. Li, and Y. Miyahara, Electrostatic moiré potential from twisted hexagonal boron nitride layers, *Nature Materials* **23**, 65 (2023).

[31] W. Kraut and R. von Baltz, Anomalous bulk photovoltaic effect in ferroelectrics: A quadratic response theory, *Physical Review B* **19**, 1548 (1979).

[32] R. von Baltz and W. Kraut, Theory of the bulk photovoltaic effect in pure crystals, *Physical Review B* **23**, 5590 (1981).

[33] T. Morimoto and N. Nagaosa, Topological nature of nonlinear optical effects in solids, *Science advances* **2**, e1501524 (2016).

[34] Q. Ma, R. Krishna Kumar, S.-Y. Xu, F. H. L. Koppens, and J. C. W. Song, Photocurrent as a multiphysics diagnostic of quantum materials, *Nature Reviews Physics* **5**, 170 (2023).

[35] A. H. Castro Neto, F. Guinea, N. M. R. Peres, K. S. Novoselov, and A. K. Geim, The electronic properties of graphene, *Reviews of Modern Physics* **81**, 109 (2009).

[36] We use a representation with the same Hamiltonian for $\pm\mathbf{K}$ -valleys of graphene.

[37] C. Ortix, L. Yang, and J. van den Brink, Graphene on incommensurate substrates: Trigonal warping and emerging dirac cone replicas with halved group velocity, *Physical Review B* **86**, 081405 (2012).

[38] J. R. Wallbank, A. A. Patel, M. Mucha-Kruczyński, A. K. Geim, and V. I. Fal'ko, Generic miniband structure of graphene on a hexagonal substrate, *Physical Review B* **87**, 245408 (2013).

[39] C.-H. Park, L. Yang, Y.-W. Son, M. L. Cohen, and S. G. Louie, Anisotropic behaviours of massless dirac fermions in graphene under periodic potentials, *Nature Physics* **4**, 213 (2008).

[40] C.-H. Park, L. Yang, Y.-W. Son, M. L. Cohen, and S. G. Louie, New generation of massless dirac fermions in graphene under external periodic potentials, *Physical Review Letters* **101**, 126804 (2008).

[41] V. V. Cheianov and V. I. Fal'ko, Selective transmission of dirac electrons and ballistic magnetoresistance of n-p junctions in graphene, *Physical Review B* **74**, 041403 (2006).

[42] V. Lukose, R. Shankar, and G. Baskaran, Novel electric field effects on landau levels in graphene, *Physical Review Letters* **98**, 116802 (2007).

[43] Z. Alisultanov, Landau levels in graphene in crossed magnetic and electric fields: Quasi-classical approach, *Physica B: Condensed Matter* **438**, 41 (2014).

[44] The Hamiltonian in vicinity of the other non-equivalent points of miniBZ, $\mu_{1,2} = \hat{R}_{2\pi/3}^{\pm 1} \mu_3$, can be obtained using $H(\mu_3 + \mathbf{q}) = H(\mu_{1,2} + \hat{R}_{2\pi/3}^{\pm 1} \mathbf{q})$.

[45] M. Yankowitz, J. Xue, D. Cormode, J. D. Sanchez-Yamagishi, K. Watanabe, T. Taniguchi, P. Jarillo-Herrero, P. Jacquod, and B. J. LeRoy, Emergence of superlattice dirac points in graphene on hexagonal boron nitride, *Nature Physics* **8**, 382 (2012).

[46] J. Callaway, *Energy band theory* (Academic Press, New York and London, 1964) chapter 4, §9.

[47] R. R. Nair, P. Blake, A. N. Grigorenko, K. S. Novoselov, T. J. Booth, T. Stauber, N. M. R. Peres, and A. K. Geim, Fine structure constant defines visual transparency of graphene, *Science* **320**, 1308 (2008).

[48] L. Ju, B. Geng, J. Horng, C. Girit, M. Martin, Z. Hao, H. A. Bechtel, X. Liang, A. Zettl, Y. R. Shen, and F. Wang, Graphene plasmonics for tunable terahertz metamaterials, *Nature Nanotechnology* **6**, 630 (2011).

[49] $\hat{T}\psi_{n,\mathbf{k}}(\mathbf{r}) = e^{i\alpha_n(\mathbf{k})}\psi_{n,-\mathbf{k}}(\mathbf{r})$, where $\alpha_n(\mathbf{k})$ is a gauge phase.

[50] L. Golub, S. Tarasenko, M. Entin, and L. Magarill, Valley separation in graphene by polarized light, *Physical Review B* **84**, 195408 (2011).

[51] In the used representation of Hamiltonian (3) the trigonal warping term is proportional to $\mp [\sigma_x(\hat{p}_x^2 - \hat{p}_y^2) - 2\sigma_y\hat{p}_x\hat{p}_y]$ for $\pm\mathbf{K}$ -valley, leading to opposite corrections to the velocity operator and zero total injection photocurrent.

[52] For σ_{ijk} , relating $j_i = \sigma_{ijk}E_jE_k^*$, there is the only independent in-plane component as $\sigma_{xxx} = -\sigma_{xyy} = -\sigma_{yxy} = -\sigma_{yyx}$.

[53] F. Ferreira, V. V. Enaldiev, V. I. Fal'ko, and S. J. Magorrian, Weak ferroelectric charge transfer in layer-asymmetric bilayers of 2D semiconductors, *Scientific Reports* **11**, 13422 (2021).

[54] V. V. Enaldiev, V. Zólyomi, C. Yelgel, S. J. Magorrian, and V. I. Fal'ko, Stacking domains and dislocation networks in marginally twisted bilayers of transition metal dichalcogenides, *Phys. Rev. Lett.* **124**, 206101 (2020).

[55] K.-A. N. Duerloo, M. T. Ong, and E. J. Reed, Intrinsic piezoelectricity in two-dimensional materials, *The Journal of Physical Chemistry Letters* **3**, 2871 (2012).

[56] H. Zhu, Y. Wang, J. Xiao, M. Liu, S. Xiong, Z. J. Wong, Z. Ye, Y. Ye, X. Yin, and X. Zhang, Observation of piezo-

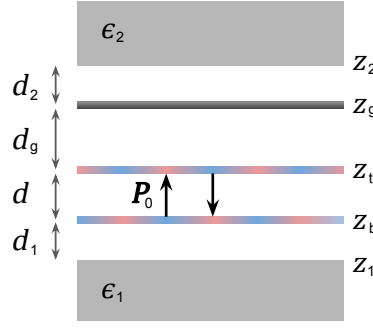


Figure S4. (a) Sketch of the electrostatic model. In the limit $\epsilon_1 \gg 1$ the bottom medium simulates proximity gate electrode that doubles electrostatic moiré potential in graphene layer (at $z = z_g$).

electricity in free-standing monolayer mos2, *Nature Nanotechnology* **10**, 151 (2014).

Supplementary Material for manuscript "Resonant absorption and linear photovoltaic effect in ferroelectric moiré heterostructures"

S1. ELECTROSTATIC MOIRÉ POTENTIAL IN GRAPHENE FROM POLAR DOMAINS IN FERROELECTRIC TWISTED BILAYER HEXAGONAL BORONE NITRIDE (HBN) OR TRANSITION METAL DICHALCOGENIDE (TMD)

In Fig. S4 we display sketch of the electrostatic model. Lattice relaxation in parallel twisted hBN and TMD bilayers results in formation of polar domains characterized by alternating (up and down) out-of-plane ferroelectric polarization. To describe the in-plane distribution of the polarization in the twisted ferroelectric bilayers, with misalignment angle θ between layers, we use the following formula [26, 53]:

$$P(\mathbf{r}) = \frac{2P_0}{3\sqrt{3}} \sum_{n=1,2,3} \sin(\mathbf{G}_n \mathbf{r}_0(\mathbf{r})), \quad (\text{S14})$$

where P_0 is the magnitude of ferroelectric polarization per unit area inside domains, $\mathbf{r}_0(\mathbf{r}) = \theta \hat{z} \times \mathbf{r} + \mathbf{u}^t - \mathbf{u}^b$ is a local interlayer lateral offset characterizing local stacking of the layers in moiré superlattice accounting of relaxation of atomic positions described by displacement fields, $\mathbf{u}^{t/b}$, in t/b layers, $\mathbf{G}_{1,2,3}$ are a triad of the shortest reciprocal vectors of a single layer related by 120° -rotation ($P_0 \approx 2.25 \times 10^{-12}$ C/m for hBN bilayers [13], and $P_0 \approx 0.6 \times 10^{-12}$ C/m for TMD bilayers [15]). The in-plane relaxation displacement fields were calculated as explained in Ref. [54] in terms of Fourier series $\mathbf{u}_{t/b}(\mathbf{r}) = \sum_n \tilde{u}_{\mathbf{g}_n} e^{i\mathbf{g}_n \cdot \mathbf{r}}$.

In the electrostatic model we suppose that ferroelectric charges, producing the polarization in domains, sit in the middle plane of the layers such that the ferroelectric charge density is

$$n_{\text{ferro}}(\mathbf{r}, z) = \frac{P(\mathbf{r})}{d} [\delta(z - z_t) - \delta(z - z_b)], \quad (\text{S15})$$

where d is interlayer distance in the bilayers. In addition to the ferroelectric charges we take into account the piezoelectric charges emerging due to inhomogeneity of in-plane strain induced by the lattice relaxation [26, 54]. The piezoelectric charge density reads as follows

$$n_{\text{piezo}}(\mathbf{r}, z) = e_{11} \sum_{l=t,b} \left[2\partial_x u_{xy}^{(l)} + \partial_y(u_{xx}^{(l)} - u_{yy}^{(l)}) \right] \delta(z - z_l), \quad (\text{S16})$$

where e_{11} is parameter of piezoelectric tensor [55, 56]. Thus, electrostatic moiré potential results from solution of the

Poisson equation:

$$\nabla \cdot [\epsilon(z) \nabla \varphi(\mathbf{r}, z)] = -4\pi e [(n_{\text{fp}}^b + n_{\text{ind}}^b) \delta(z - z_b) + (n_{\text{fp}}^t + n_{\text{ind}}^t) (\mathbf{r}) \delta(z - z_t) + n_{\text{ind}}^{gr}(\mathbf{r}) \delta(z - z_g)]. \quad (\text{S17})$$

$$\epsilon(z) = \begin{cases} \epsilon_2, & z > z_2 \\ 1, & z_1 < z < z_2 \\ \epsilon_1, & z < z_1 \end{cases} \quad (\text{S18})$$

Here, $\nabla = (\partial/\partial \mathbf{r}, \partial/\partial z)$ and 2D densities are defined as follows:

$$n_{\text{fp}}^{t/b} = \pm \frac{P(\mathbf{r})}{d} + e_{11} \left[2\partial_x u_{xy}^{(t/b)} + \partial_y(u_{xx}^{(t/b)} - u_{yy}^{(t/b)}) \right], \quad (\text{S19})$$

$$n_{\text{ind}}^{t/b} = -\alpha \left(\frac{\partial^2}{\partial x^2} + \frac{\partial^2}{\partial y^2} \right) \varphi(\mathbf{r}, z_{t/b}) \quad (\text{S20})$$

$$n_{\text{ind}}^{gr}(\mathbf{r}) = e \int d^3 \mathbf{r}' \Pi(\mathbf{r} - \mathbf{r}', k_F) \varphi(\mathbf{r}', z_{gr}). \quad (\text{S21})$$

Equations (S20) and (S21) describe induced polarization charges in t/b layer and graphene, respectively, which are determined by 2D polarizability, $\alpha = d(\epsilon_{||} - 1)/4\pi$ (where $\epsilon_{||}$ is in-plane dielectric permittivity of bulk TMD/hBN crystal), and polarization operator of massless Dirac fermions in graphene, $\Pi(\mathbf{r} - \mathbf{r}', k_F)$ with the Fermi-wave number determined as $k_F = \sqrt{\pi n}$ (n is carrier concentration) [35]. Looking for solution of Eq. (S17) in terms of a Fourier series $\varphi(\mathbf{r}, z) = \sum_{\mathbf{g}_n} (\varphi_n(z) e^{i\mathbf{g}_n \cdot \mathbf{r}} + \text{c.c.})$ with continuity boundary conditions for potential and corresponding break for out-of-plane component of electric field at each interface we obtain the following expression for the potential harmonic in graphene layer:

$$\varphi_n(z_g) = \frac{\frac{4\pi}{g_n} \{ n_n^t [\Theta_n(d + d_1, \epsilon_1) + 4\pi\alpha g_n \text{sh}(g_n d) \Theta_n(d_1, \epsilon_1)] + n_n^b \Theta_n(d_1, \epsilon_1) \} \Theta_n(d_2, \epsilon_2)}{\begin{vmatrix} \Phi_n(d_2, \epsilon_2) + \frac{4\pi\epsilon^2}{g_n} \Pi(g_n, k_F) \Theta_n(d_2, \epsilon_2) & \Xi_n \\ -\Theta_n(d_2, \epsilon_2) & \Lambda_n \end{vmatrix}} \quad (\text{S22})$$

where $n_n^{t/b}$ is corresponding Fourier harmonic of the 2D charge density in t/b layer (S19) and we introduced the following functions:

$$\begin{aligned} \Theta_n(d, \epsilon) &= \text{ch}(g_n d) + \epsilon \text{sh}(g_n d), \\ \Phi_n(d, \epsilon) &= \epsilon \text{ch}(g_n d) + \text{sh}(g_n d), \end{aligned}$$

$$\Xi_n = \Phi_n(d + d_1 + d_g, \epsilon_1) + 4\pi\alpha g_n \text{ch}(g_n(d + d_g)) \Theta_n(d_1, \epsilon_1) + 4\pi\alpha g_n \text{ch}(g_n d_g) [\Theta_n(d + d_1, \epsilon_1) + 4\pi\alpha g_n \text{sh}(g_n d) \Theta_n(d_1, \epsilon_1)],$$

$$\Lambda_n = \Theta_n(d + d_1 + d_g, \epsilon_1) + 4\pi\alpha g_n \text{sh}(g_n(d + d_g)) \Theta_n(d_1, \epsilon_1) + 4\pi\alpha g_n \text{sh}(g_n d_g) [\Theta_n(d + d_1, \epsilon_1) + 4\pi\alpha g_n \text{sh}(g_n d) \Theta_n(d_1, \epsilon_1)].$$

In Table S1 we gathered values of the potential harmonics values for graphene/twisted hBN bilayer heterostructure with $\theta = 0.18^\circ$ and different electron concentrations.

Table S1. Non-zero harmonics of electrostatic moiré potential in graphene layer of graphene/twisted hBN heterostructure studied in the main text $V_n^{(a)} = -|e|\varphi_n(z_g)$ (in meV) at three values of electron concentration (in cm^{-2}). The value were calculated at the following parameters $a = 2.5 \text{ \AA}$, $d = 3.35 \text{ \AA}$; $d_1 = 3.35 \text{ \AA}$; $d_2 = 3.34 \text{ \AA}$; $d_g = 3.325 \text{ \AA}$, $\epsilon_1 = \infty$, $\epsilon_2 = 3.5$ and $\alpha \approx 0.93 \text{ \AA}$. Due to 120° -rotational symmetry of potential, harmonics φ_n for reciprocal vectors with the same magnitude (i.e. $\mathbf{g}_{2,3}^{(n)} = \hat{R}_z(\pm \frac{2\pi}{3}) \mathbf{g}_1^{(n)}$; $\hat{R}_z(\pm \frac{2\pi}{3})$ is $\pm 120^\circ$ -rotation matrix) are equal to that of $\mathbf{g}_1^{(n)}$. Here $\mathbf{g}_1^{(1)} = (4\pi\theta/a\sqrt{3})(1/2, \sqrt{3}/2)$.

g_n	10^{10} cm^{-2}	10^{11} cm^{-2}	10^{12} cm^{-2}
$\mathbf{g}_1^{(1)}$	42.875	31.946	16.533
$\mathbf{g}_1^{(3)} = 2\mathbf{g}_1^{(1)}$	13.59	11.998	6.589
$\mathbf{g}_1^{(6)} = 3\mathbf{g}_1^{(1)}$	5.598	5.219	3.202
$\mathbf{g}_1^{(10)} = 4\mathbf{g}_1^{(1)}$	2.49	2.356	1.564
$\mathbf{g}_1^{(15)} = 5\mathbf{g}_1^{(1)}$	1.11	1.059	0.756
$\mathbf{g}_1^{(21)} = 6\mathbf{g}_1^{(1)}$	0.459	0.441	0.35
$\mathbf{g}_1^{(29)} = 7\mathbf{g}_1^{(1)}$	0.167	0.161	0.139
$\mathbf{g}_1^{(40)} = 8\mathbf{g}_1^{(1)}$	0.042	0.041	0.037
$\mathbf{g}_1^{(50)} = 9\mathbf{g}_1^{(1)}$	0.004	0.003	0.002

S2. EFFECTIVE HAMILTONIAN FOR PRIMARY MASSLESS DIRAC FERMIONS

To obtain Hamiltonian H_γ (Eq. (3) in the main manuscript) we, first, project out Hamiltonian $\hat{H}_0 = v\boldsymbol{\sigma} \cdot \hat{\mathbf{p}} + V(\mathbf{r})$ on a set of plane waves corresponding to the lowest Fourier harmonics ($\mathbf{g}_{1,2,3} \equiv \mathbf{g}_{1,2,3}^{(1)}$) of the moiré potential: $\psi \approx e^{i\mathbf{k}\mathbf{r}} \left(\tilde{\psi}_0 + \sum_{l=1,2,3} \left[\tilde{\psi}_{\mathbf{g}_l} e^{i\mathbf{g}_l \cdot \mathbf{r}} + \tilde{\psi}_{-\mathbf{g}_l} e^{-i\mathbf{g}_l \cdot \mathbf{r}} \right] \right)$, leading to

$$\begin{pmatrix} \hbar v \boldsymbol{\sigma} \cdot \mathbf{k} & -\frac{V_1^{(a)}}{2i} \sigma_0 & \frac{V_1^{(a)}}{2i} \sigma_0 & -\frac{V_1^{(a)}}{2i} \sigma_0 & \frac{V_1^{(a)}}{2i} \sigma_0 & -\frac{V_1^{(a)}}{2i} \sigma_0 & \frac{V_1^{(a)}}{2i} \sigma_0 \\ \frac{V_1^{(a)}}{2i} \sigma_0 & \hbar v \boldsymbol{\sigma} \cdot (\mathbf{k} + \mathbf{g}_1) & 0 & 0 & 0 & 0 & 0 \\ -\frac{V_1^{(a)}}{2i} \sigma_0 & 0 & \hbar v \boldsymbol{\sigma} \cdot (\mathbf{k} - \mathbf{g}_1) & 0 & 0 & 0 & 0 \\ \frac{V_1^{(a)}}{2i} \sigma_0 & 0 & 0 & \hbar v \boldsymbol{\sigma} \cdot (\mathbf{k} + \mathbf{g}_2) & 0 & 0 & 0 \\ -\frac{V_1^{(a)}}{2i} \sigma_0 & 0 & 0 & 0 & \hbar v \boldsymbol{\sigma} \cdot (\mathbf{k} - \mathbf{g}_2) & 0 & 0 \\ \frac{V_1^{(a)}}{2i} \sigma_0 & 0 & 0 & 0 & 0 & \hbar v \boldsymbol{\sigma} \cdot (\mathbf{k} + \mathbf{g}_3) & 0 \\ -\frac{V_1^{(a)}}{2i} \sigma_0 & 0 & 0 & 0 & 0 & 0 & \hbar v \boldsymbol{\sigma} \cdot (\mathbf{k} - \mathbf{g}_3) \end{pmatrix} \begin{pmatrix} \tilde{\psi}_0 \\ \tilde{\psi}_{\mathbf{g}_1} \\ \tilde{\psi}_{-\mathbf{g}_1} \\ \tilde{\psi}_{\mathbf{g}_2} \\ \tilde{\psi}_{-\mathbf{g}_2} \\ \tilde{\psi}_{\mathbf{g}_3} \\ \tilde{\psi}_{-\mathbf{g}_3} \end{pmatrix} = \varepsilon \begin{pmatrix} \tilde{\psi}_0 \\ \tilde{\psi}_{\mathbf{g}_1} \\ \tilde{\psi}_{-\mathbf{g}_1} \\ \tilde{\psi}_{\mathbf{g}_2} \\ \tilde{\psi}_{-\mathbf{g}_2} \\ \tilde{\psi}_{\mathbf{g}_3} \\ \tilde{\psi}_{-\mathbf{g}_3} \end{pmatrix}. \quad (\text{S23})$$

where we take into account only matrix elements between $\tilde{\psi}_0$ and $\tilde{\psi}_{\mathbf{g}_l \neq 0}$, whereas those between $\tilde{\psi}_{\mathbf{g}_l \neq 0}$ were neglected. For $\mathbf{k} = 0$ two eigen states of matrix (S23) possesses zero energy:

$$\tilde{\psi}_{+1} = \frac{1}{\sqrt{6 + \left(\frac{2\hbar v |\mathbf{g}_1|}{V_1^{(a)}} \right)^2}} \begin{pmatrix} \frac{2\hbar v |\mathbf{g}_1|}{V_1^{(a)}}, 0, 0, e^{i\frac{2\pi}{3}}, 0, e^{i\frac{2\pi}{3}}, 0, -e^{i\frac{\pi}{3}}, 0, -e^{i\frac{\pi}{3}}, 0, 1, 0, 1 \end{pmatrix}^T, \quad (\text{S24})$$

$$\tilde{\psi}_{-1} = \frac{1}{\sqrt{6 + \left(\frac{2\hbar v |\mathbf{g}_1|}{V_1^{(a)}} \right)^2}} \begin{pmatrix} 0, \frac{2\hbar v |\mathbf{g}_1|}{V_1^{(a)}}, e^{-i\frac{2\pi}{3}}, 0, -e^{i\frac{\pi}{3}}, 0, e^{i\frac{2\pi}{3}}, 0, e^{i\frac{2\pi}{3}}, 0, 1, 0, 1, 0 \end{pmatrix}^T. \quad (\text{S25})$$

Projecting the Hamiltonian with $\mathbf{k} \neq 0$ onto subspace of the zero energy states: $\psi = C_1(\mathbf{k})\tilde{\psi}_{+1} + C_2(\mathbf{k})\tilde{\psi}_{-1}$, we arrive to the following effective model:

$$\begin{pmatrix} 0 & \frac{\hbar v}{1 + \frac{3}{2} \left(\frac{V_1^{(a)}}{\hbar v |\mathbf{g}_1|} \right)^2} (k_x - ik_y) \\ \frac{\hbar v}{1 + \frac{3}{2} \left(\frac{V_1^{(a)}}{\hbar v |\mathbf{g}_1|} \right)^2} (k_x + ik_y) & 0 \end{pmatrix} \begin{pmatrix} C_1 \\ C_2 \end{pmatrix} = \varepsilon \begin{pmatrix} C_1 \\ C_2 \end{pmatrix}. \quad (\text{S26})$$

Substituting $|\mathbf{g}_1| = 4\pi\theta/a\sqrt{3}$ in the left-hand side of Eq. (S26) we obtain \hat{H}_γ from the main text.

S3. EFFECTIVE HAMILTONIAN FOR SECONDARY MASSLESS DIRAC FERMIONS

Secondary Dirac fermions emerge in vicinity of $\mathbf{k} = \mathbf{g}_{1,2,3}/2 = \boldsymbol{\mu}_{1,2,3}$. Due to 120° -rotational symmetry it is enough to derive effective Hamiltonian for $\boldsymbol{\mu}_3 = (g_1/2, 0)$, that can be obtained leaving only the first and last lines in the left-hand side of Eq. (S23) (i.e. approximating $\psi \approx e^{i\mathbf{k}\mathbf{r}} \left(\tilde{\psi}_0 + \tilde{\psi}_{\mathbf{g}_3} e^{-i\mathbf{g}_3 \cdot \mathbf{r}} \right)$) and putting $\mathbf{k} = \mathbf{q} + \mathbf{g}_3/2$. This leads to:

$$\hat{H} = \begin{pmatrix} \frac{\hbar v g_1}{2} \sigma_x + \hbar v \boldsymbol{\sigma} \cdot \mathbf{q} & \frac{V_1^{(a)}}{2i} \sigma_0 \\ \frac{V_1^{(a)}}{2i} \sigma_0 & -\frac{\hbar v g_1}{2} \sigma_x + \hbar v \boldsymbol{\sigma} \cdot \mathbf{q} \end{pmatrix}. \quad (\text{S27})$$

Applying unitary transformation \hat{U} to \hat{H} we obtain

$$\hat{\tilde{H}} = \hat{U} \hat{H} \hat{U}^+ = \begin{pmatrix} \varepsilon_{\mu} + \hbar v \sigma_z q_y \frac{V_1^{(a)}}{2\varepsilon_{\mu}} - \hbar v \sigma_x q_x & i \frac{\hbar v g_1}{2\varepsilon_{\mu}} \hbar v \sigma_z q_y \\ -i \frac{g_1}{2\varepsilon_{\mu}} \sigma_z q_y & -\varepsilon_{\mu} - \hbar v \sigma_z q_y \frac{V_1^{(a)}}{2\varepsilon_{\mu}} - \hbar v \sigma_x q_x \end{pmatrix} \quad (\text{S28})$$

where

$$\hat{U} = \frac{1}{2} \begin{pmatrix} 1 & \frac{1}{2} \frac{\hbar v g_1 - i V_1^{(a)}}{\varepsilon_{\mu}} & \frac{1}{2} \frac{\hbar v g_1 - i V_1^{(a)}}{\varepsilon_{\mu}} & -1 \\ -\frac{1}{2} \frac{\hbar v g_1 - i V_1^{(a)}}{\varepsilon_{\mu}} & -1 & 1 & -\frac{1}{2} \frac{\hbar v g_1 - i V_1^{(a)}}{\varepsilon_{\mu}} \\ 1 & -\frac{1}{2} \frac{\hbar v g_1 - i V_1^{(a)}}{\varepsilon_{\mu}} & -\frac{1}{2} \frac{\hbar v g_1 - i V_1^{(a)}}{\varepsilon_{\mu}} & -1 \\ \frac{1}{2} \frac{\hbar v g_1 - i V_1^{(a)}}{\varepsilon_{\mu}} & -1 & 1 & \frac{1}{2} \frac{\hbar v g_1 - i V_1^{(a)}}{\varepsilon_{\mu}} \end{pmatrix} \quad (\text{S29})$$

and $\varepsilon_{\mu} = (1/2) \sqrt{(\hbar v g_1)^2 + (V_1^{(a)})^2}$. Next, we consider eigenvalue problem for Hamiltonian (S28):

$$\begin{pmatrix} \varepsilon_{\mu} + \hbar v \sigma_z q_y \frac{V_1^{(a)}}{2\varepsilon_{\mu}} - \hbar v \sigma_x q_x & i \frac{\hbar v g_1}{2\varepsilon_{\mu}} \hbar v \sigma_z q_y \\ -i \frac{g_1}{2\varepsilon_{\mu}} \sigma_z q_y & -\varepsilon_{\mu} - \hbar v \sigma_z q_y \frac{V_1^{(a)}}{2\varepsilon_{\mu}} - \hbar v \sigma_x q_x \end{pmatrix} \begin{pmatrix} \psi_+ \\ \psi_- \end{pmatrix} = \varepsilon \begin{pmatrix} \psi_+ \\ \psi_- \end{pmatrix} \quad (\text{S30})$$

and express ψ_- via ψ_+ (ψ_+ via ψ_-) for states characterized by energies in vicinity of secondary Dirac point $\varepsilon \approx \varepsilon_{\mu}$ ($\varepsilon \approx -\varepsilon_{\mu}$). This leads us to the following equation:

$$\left[\pm \varepsilon_{\mu} \pm \hbar v \sigma_z q_y \frac{V_1^{(a)}}{2\varepsilon_{\mu}} \pm \frac{(\hbar v g_1)^2}{8\varepsilon_{\mu}^3} (\hbar v q_y)^2 - \hbar v \sigma_x q_x \right] \psi_{\pm} = \varepsilon \psi_{\pm}. \quad (\text{S31})$$

After exchange $v \rightarrow v_*$ in the left-hand side of Eq. (S31) (which, as we checked, gives better approximation to exact dispersion) we arrive to the Hamiltonian for secondary Dirac fermions introduced in the main text.

S4. MINIBAND STRUCTURE IN GRAPHENE/TWISTED FERROELECTRIC BILAYER AT FINITE OUT-OF-PLANE ELECTRIC FIELD ACROSS POLAR DOMAINS

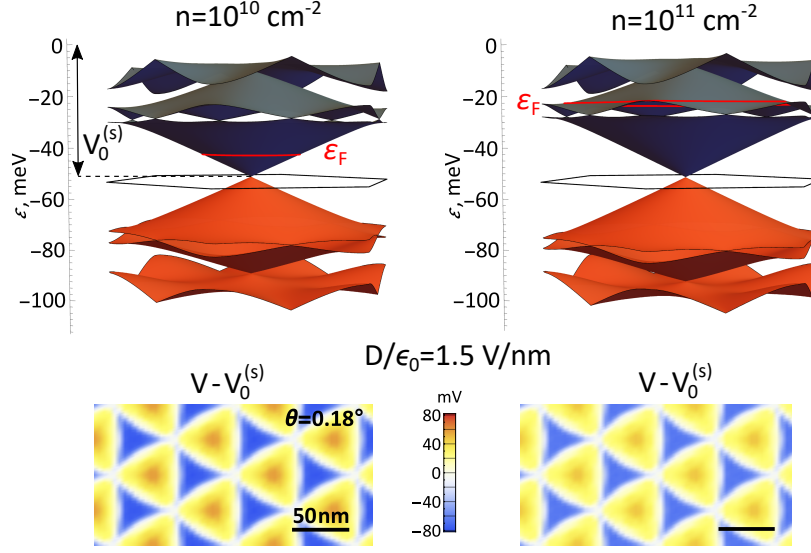


Figure S5. (a) Mini-band structures in graphene/twisted hBN bilayer at out-of-plane electric field $D/\epsilon_0 = 1.5$ V/nm across the twisted interface with $\theta = 0.18^\circ$. Bottom inset show polar domain structure for the electric field.

S5. RESONANT ABSORPTION AND SHIFT PHOTOCURRENT AT FINITE OUT-OF-PLANE ELECTRIC FIELD ACROSS TWISTED INTERFACE

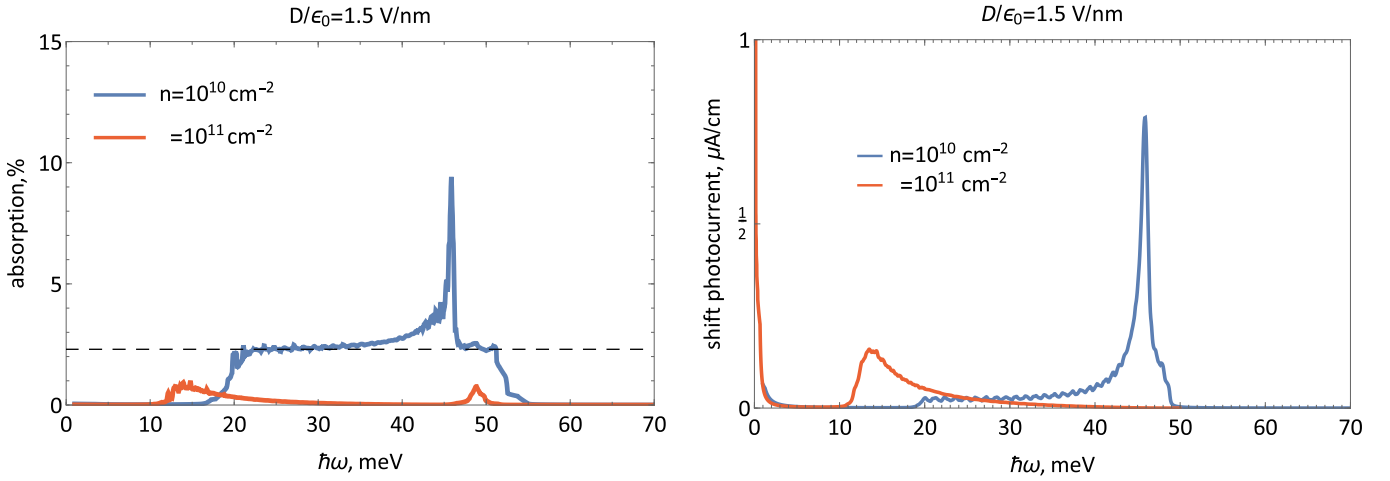


Figure S6. (a) Frequency dependences of absorption (left) and shift photocurrent (right) for graphene/twisted hBN bilayer heterostructure at out-of-plane electric field $D/\epsilon_0 = 1.5$ V/nm across the twisted interface and $\theta = 0.18^\circ$. The shift photocurrent was calculated at the intensity of incident radiation, $I = 0.1$ W/cm². Dashed line on the left panel shows absorption of isolated graphene $\approx 2.3\%$.

S6. DERIVATION OF THE INJECTION AND SHIFT PHOTOCURRENTS

In this section we derive equations (8)-(10) in the main text. For that we consider the following Hamiltonian:

$$\hat{H} = \hat{H}_0 + \hat{H}_1(t), \quad (\text{S32})$$

$$\hat{H}_0 = v\boldsymbol{\sigma} \cdot \hat{\mathbf{p}} + V(\mathbf{r}), \quad (\text{S33})$$

$$\hat{H}_1(t) = v\boldsymbol{\sigma} \cdot \mathbf{A}(t) = \frac{A_0}{2} v\boldsymbol{\sigma} \cdot \boldsymbol{\eta} (e^{i\omega t + \gamma t} + e^{-i\omega t + \gamma t}), \quad (\text{S34})$$

where we keep designations introduced in the main text and add $\gamma > 0$ ($\gamma \ll \omega$) assuming vanishing of the wave at $t \rightarrow -\infty$. Then, we look for density matrix as a series $\hat{\rho} = \hat{\rho}_0 + \hat{\rho}_1 + \hat{\rho}_2$, where $\hat{\rho}_0 = \sum_{n,\mathbf{k}} f(\varepsilon_n(\mathbf{k})) |n\mathbf{k}\rangle \langle n\mathbf{k}|$ is equilibrium density matrix ($\langle \mathbf{r} | n\mathbf{k} \rangle \equiv \psi_{n\mathbf{k}}(\mathbf{r})$ is Bloch state), while $\hat{\rho}_1 \propto A_0$ and $\hat{\rho}_2 \propto A_0^2$. To determine the first and second amendments to equilibrium density matrix we perturbatively solve Liouville equation:

$$\frac{\partial(\hat{\rho}_1 + \hat{\rho}_2)}{\partial t} = \frac{i}{\hbar} [\hat{H}_0 + \hat{H}_1, \hat{\rho}_0 + \hat{\rho}_1 + \hat{\rho}_2]. \quad (\text{S35})$$

From Eq. (S35) we find

$$\hat{\rho}_2 = \frac{1}{(i\hbar)^2} \int_{-\infty}^t dt' \int_{-\infty}^{t'} dt'' e^{\frac{-i}{\hbar} \hat{H}_0(t-t')} [\hat{H}_1(t'), e^{\frac{-i}{\hbar} \hat{H}_0(t'-t'')} [\hat{H}_1(t''), \hat{\rho}_0] e^{\frac{i}{\hbar} \hat{H}_0(t'-t'')}] e^{\frac{i}{\hbar} \hat{H}_0(t-t')}. \quad (\text{S36})$$

Matrix element on the Bloch states for zero-frequency part of density operator (S36) reads as follows:

$$\langle n'\mathbf{k} | \hat{\rho}_2 | n\mathbf{k} \rangle = \frac{e^2 A_0^2}{4} \sum_{\substack{\Omega=\pm\hbar\omega \\ n''}} \frac{(\mathbf{v}_{n'n''}(\mathbf{k}) \cdot \boldsymbol{\eta})(\mathbf{v}_{n''n}(\mathbf{k}) \cdot \boldsymbol{\eta})}{\varepsilon_{n'}(\mathbf{k}) - \varepsilon_n(\mathbf{k}) - i\gamma} \left[\frac{f(\varepsilon_n(\mathbf{k})) - f(\varepsilon_{n''}(\mathbf{k}))}{\varepsilon_{n''}(\mathbf{k}) - \varepsilon_n(\mathbf{k}) - \Omega - i\gamma} + \frac{f(\varepsilon_{n'}(\mathbf{k})) - f(\varepsilon_{n''}(\mathbf{k}))}{\varepsilon_{n'}(\mathbf{k}) - \varepsilon_{n''}(\mathbf{k}) - \Omega - i\gamma} \right] \quad (\text{S37})$$

where $\mathbf{v}_{nn'}(\mathbf{k}) = \langle n\mathbf{k} | v\boldsymbol{\sigma} | n'\mathbf{k} \rangle$ is velocity operator matrix element.

Calculating current with the help of Eq. (S37) we obtain:

$$\begin{aligned} \mathbf{j} &= \frac{e}{S} \sum_{n,\mathbf{k}} \langle n\mathbf{k} | v\boldsymbol{\sigma} \hat{\rho}_2 | n\mathbf{k} \rangle = \frac{e}{S} \sum_{n,n',\mathbf{k}} \langle n\mathbf{k} | v\boldsymbol{\sigma} | n'\mathbf{k} \rangle \langle n'\mathbf{k} | \hat{\rho}_2 | n\mathbf{k} \rangle = \\ &= \frac{e^3 A_0^2}{4S} \sum_{\substack{\Omega=\pm\hbar\omega \\ n'',n',n,\mathbf{k}}} \frac{\mathbf{v}_{nn'}(\mathbf{k})(\mathbf{v}_{n'n''}(\mathbf{k}) \cdot \boldsymbol{\eta})(\mathbf{v}_{n''n}(\mathbf{k}) \cdot \boldsymbol{\eta})}{\varepsilon_{n'}(\mathbf{k}) - \varepsilon_n(\mathbf{k}) - i\gamma} \left[\frac{f(\varepsilon_n(\mathbf{k})) - f(\varepsilon_{n''}(\mathbf{k}))}{\varepsilon_{n''}(\mathbf{k}) - \varepsilon_n(\mathbf{k}) - \Omega - i\gamma} + \frac{f(\varepsilon_{n'}(\mathbf{k})) - f(\varepsilon_{n''}(\mathbf{k}))}{\varepsilon_{n'}(\mathbf{k}) - \varepsilon_{n''}(\mathbf{k}) - \Omega - i\gamma} \right] \\ &= \frac{e^3 A_0^2}{4S} \sum_{\substack{\Omega=\pm\hbar\omega \\ n'',n',n,\mathbf{k}}} \frac{\mathbf{v}_{nn}(\mathbf{k})(\mathbf{v}_{nn''}(\mathbf{k}) \cdot \boldsymbol{\eta})(\mathbf{v}_{n''n}(\mathbf{k}) \cdot \boldsymbol{\eta})}{-i\gamma} \left(\frac{f(\varepsilon_n(\mathbf{k})) - f(\varepsilon_{n''}(\mathbf{k}))}{\varepsilon_{n''}(\mathbf{k}) - \varepsilon_n(\mathbf{k}) - \Omega - i\gamma} - \frac{f(\varepsilon_n(\mathbf{k})) - f(\varepsilon_{n''}(\mathbf{k}))}{\varepsilon_{n''}(\mathbf{k}) - \varepsilon_n(\mathbf{k}) - \Omega + i\gamma} \right) + \\ &+ \frac{e^3 A_0^2}{4S} \sum_{\substack{\Omega=\pm\hbar\omega \\ n'',n',\neq n,\mathbf{k}}} \frac{f(\varepsilon_n(\mathbf{k})) - f(\varepsilon_{n''}(\mathbf{k}))}{\varepsilon_{n'}(\mathbf{k}) - \varepsilon_n(\mathbf{k})} \left[\frac{\mathbf{v}_{nn'}(\mathbf{k})(\mathbf{v}_{n'n''}(\mathbf{k}) \cdot \boldsymbol{\eta})(\mathbf{v}_{n''n}(\mathbf{k}) \cdot \boldsymbol{\eta})}{\varepsilon_{n''}(\mathbf{k}) - \varepsilon_n(\mathbf{k}) - \Omega - i\gamma} + \frac{\mathbf{v}_{nn'}^*(\mathbf{k})(\mathbf{v}_{n'n''}^*(\mathbf{k}) \cdot \boldsymbol{\eta})(\mathbf{v}_{n''n}^*(\mathbf{k}) \cdot \boldsymbol{\eta})}{\varepsilon_{n''}(\mathbf{k}) - \varepsilon_n(\mathbf{k}) - \Omega + i\gamma} \right] \end{aligned} \quad (\text{S38})$$

Applying Sokhotski-Plemelj formula and replacing $\gamma \rightarrow \hbar/\tau$ in the first term ($n' = n$) after the last equality in Eq. (S38) we obtain the expression for the injection photocurrent in the main manuscript:

$$j_{\text{inj}} = \frac{e^3 A_0^2 \pi \tau}{2\hbar S} \sum_{\substack{\Omega=\pm\hbar\omega \\ n'',n,\mathbf{k}}} \mathbf{v}_{nn}(\mathbf{k})(\mathbf{v}_{nn''}(\mathbf{k}) \cdot \boldsymbol{\eta})(\mathbf{v}_{n''n}(\mathbf{k}) \cdot \boldsymbol{\eta}) [f(\varepsilon_{n''}(\mathbf{k})) - f(\varepsilon_n(\mathbf{k}))] \delta(\varepsilon_{n''}(\mathbf{k}) - \varepsilon_n(\mathbf{k}) - \Omega), \quad (\text{S39})$$

whereas the second term transforms into the expression for the shift photocurrent by virtue of $\mathbf{v}_{n'n}(\mathbf{k}) = -e^{i\alpha_n(\mathbf{k}) - i\alpha_{n'}(\mathbf{k})} \mathbf{v}_{n'n}^*(-\mathbf{k})$ and $\varepsilon_n(-\mathbf{k}) = \varepsilon_n(\mathbf{k})$ imposed by the hidden symmetry $\hat{T} = i\sigma_y \hat{K}$ and taking the limit $\gamma \rightarrow +0$. This leads to

$$j_{\text{shift}} = \frac{e^3 A_0^2 \pi}{2S} \sum_{\substack{\Omega=\pm\hbar\omega \\ n'',n',\neq n,\mathbf{k}}} \frac{f(\varepsilon_n(\mathbf{k})) - f(\varepsilon_{n''}(\mathbf{k}))}{\varepsilon_{n'}(\mathbf{k}) - \varepsilon_n(\mathbf{k})} \delta(\varepsilon_{n''}(\mathbf{k}) - \varepsilon_n(\mathbf{k}) - \Omega) \text{Im} [\mathbf{v}_{nn'}(\mathbf{k})(\mathbf{v}_{n'n''}(\mathbf{k}) \cdot \boldsymbol{\eta})(\mathbf{v}_{n''n}(\mathbf{k}) \cdot \boldsymbol{\eta})]. \quad (\text{S40})$$